ASTRONOMY & ASTROPHYSICS
SUPPLEMENT SERIES

JUNE II **2000**, PAGE 523

Astron. Astrophys. Suppl. Ser. **144**, 523–532 (2000)

Adaptive optics imaging of P Cygni in H_α ⋆

O. Chesneau[1], M. Roche[2], A. Boccaletti[3], L. Abe[1], C. Moutou[4], F. Charbonnier[5], C. Aime[2], H. Lantéri[2], and F. Vakili[1]

[1] Observatoire de la Côte d'Azur, Département Fresnel, GI2T, F-06460 Saint Vallier de Thiey, France
[2] UMR 6525 Astrophysique, Université de Nice Sophia Antipolis Parc Valrose, F-06108 Nice Cedex 2, France
[3] Collège de France, 11 Pl. M. Berthelot, F-75321 Paris, France
[4] European Southern Observatory, Alonso de Cordoba 3107, Santiago, Chile
[5] Office National d'Études et de Recherches Aérospatiales, Département d'Optique Théorique et Appliquée Imagerie Haute Résolution - Optique Adaptative, 29 Av. de la Division Leclerc, F-92320 Chatillon, France

Received January 10; accepted March 20, 2000

Abstract. We obtained H_α diffraction limited data of the LBV star P Cyg using the ONERA Adaptive Optics (AO) facility BOA at the OHP 1.52 m telescope on October 1997. Taking P Cyg and the reference star 59 Cyg AO long exposures, we find that P Cyg clearly exhibits a large and diffuse intensity distribution compared to the 59 Cyg's point-like source. A deconvolution of P Cyg using 59 Cyg as the Point Spread Function was performed by means of the Richardson-Lucy algorithm. P Cyg clearly appears as an unresolved star surrounded by a clumped envelope. The reconstructed image of P Cyg is compared to similar spatial resolution maps obtained from radio aperture synthesis imaging. We put independent constraints on the physics of P Cyg which agree well with radio results. We discuss future possibilities to constrain the wind structure of P Cyg by using multi-resolution imaging, coronagraphy and long baseline interferometry to trace back its evolutionary status.

Key words: star: P Cyg — stars: winds, imaging, circumstellar matter — instrumentation: adaptive optics

1. Introduction

Among the galactic Luminous Blue Variables (LBV), the supergiant P Cyg (HD 193237, B1Ia+) is both a historical prototype since its famous XVIIth century eruptions, and an intriguing paradigm in many aspects. In their exhaustive study of P Cyg's fundamental parameters, mass loss physics and evolution, Nota et al. (Nota et al. 1995) have claimed this star as being the unique case of the so-called "Peculiar Nebulae" class LBVs. Indeed, the 22 arcseconds (arcsec) faint and spherical nebulae around P Cyg, were only recently discovered by Barlow et al. (Barlow et al. 1994) who estimate its mass as 0.01 $M_\odot$. This value differs significantly from those of more regular LBVs, ranging from 1 $M_\odot$ to 4.2 $M_\odot$ (e.g. for AG Car) which also present more asymmetric nebula.

Evolutive tracks suggest an initial mass of 48 ± 6 $M_\odot$, and its present mass is estimated to be at the most 40 $M_\odot$, but lower masses ($\sim$ 30 $M_\odot$) are also reported in literature (Lamers et al. 1983; Lamers et al. 1985; Turner et al. 1999). However, the fine spatial structure of this large amount of excreted matter remains to be detailed. P Cyg's relative proximity ($\sim$ 1.8 kpc, Lamers et al. 1983) represents an opportunity to observe its radiatively driven mass loss from the starting point out to the interstellar medium. Indeed, at 1.8 kpc, the central star radius (76 $R_\odot$) corresponds to a tiny angle of 0.2 milliarcsecond (mas) but the H_α emitting region extends over several tens of arcsecs, and radio emission seems to attain even larger scales (Meaburn et al. 1999). The optical and radio observations reported to date, depict an essentially clumpy distribution of matter, both at large (Taylor et al. 1991; Nota et al. 1995) and small scales (Skinner et al. 1998; Vakili et al. 1997), with temporally variable emission (Skinner et al. 1997). These imaging observations remain sparse and can loosely constrain the spatial and/or temporal evolution of the clumps in the nebula. Moreover, in the optical wavelengths, the star to envelope brightness ratio remains an obstacle for studying the immediate environment of the central star. In this paper we report an attempt to observe the H_α circumstellar environment of P Cyg during an AO run

Send offprint requests to: O. Chesneau

⋆ Based on data collected at the Observatoire de Haute-Provence.

Correspondence to: chesneau@astro.umontreal.ca

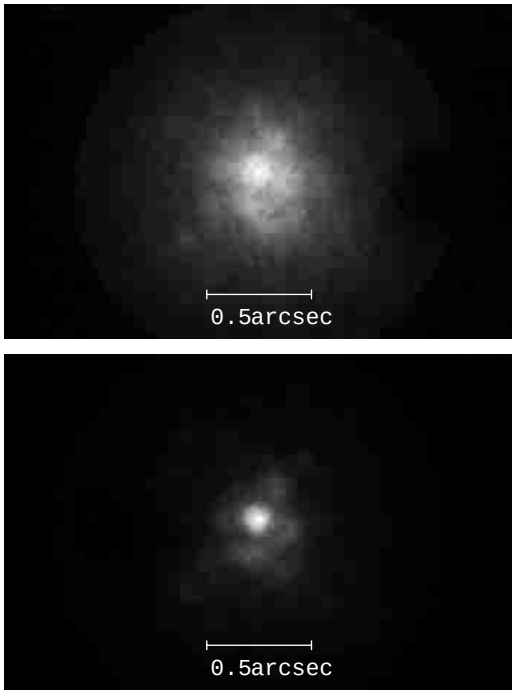

Fig. 1. H_α long exposures of P Cyg (top) and the reference star 59 Cyg (bottom) recorded with the CP20 camera at OHP during October 4th 1997 using the AO system BOA from ONERA through a filter ($\Delta\lambda = 10$ nm). The images are smoothed using a moving average window of 4×4 pixels. Note that the theoretical angular resolution of the 1.52 m telescope at 6563 Å ($1.22\lambda/D = 0.110$ arcsec) is closely reached (broken first Airy ring is visible on 59 Cyg) whilst for P Cyg a more complex and resolved structure can be suspected

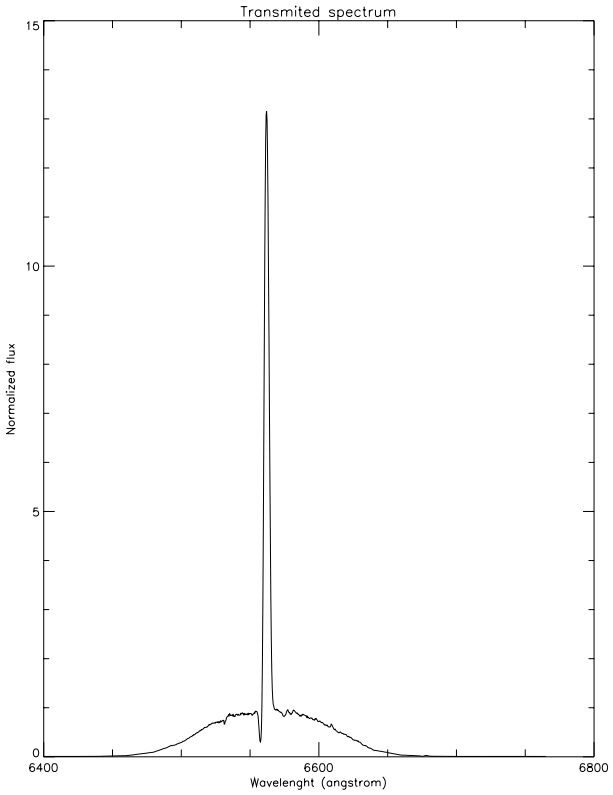

Fig. 2. Synthetic representation of the H_α region of P Cyg multiplied by the filter transmission used for the adaptive optics imaging of P Cyg. The same filter was used for 59 Cyg. About 45.6% of the transmitted light originates from the line continuum

at the OHP observatory on October 1997 using short exposures collected with a photon-counting camera.

The paper is organized as follows. In Sect. 2, we describe the AO+imaging instrumentation used for this study as well as data reduction and calibration procedures. Section 3 describes the image reconstruction in which particular efforts have been made to test the validity of the PSF. The last section makes a critical discussion of our findings, and attention is given on the perspectives opened by the emergencies of new high angular resolution techniques. A need arises for a coordinated campaign for a global approach of P Cyg, and LBVs environment.

2. Journal of observations

2.1. Instrumentation

P Cyg was observed, in the context of a dark-speckle run (Boccaletti et al. 1998). The AO bench of the ONERA (Office National d'Études et de Recherches Aérospatiales) was installed at the Coudé focus of the 1.52 m telescope. The 90 actuators of BOA and its 1 kHz closed loop bandwidth enable a compensation of atmospheric turbulence in visible light (Conan et al. 1998) and provide typical Strehl ratio of 10% to 30% depending on seeing conditions.

The restored wavefront feeds a dark-speckle optics designed to detect faint companions around bright objects. The beam is then focused onto the detector with an $f/976$ aperture, giving a fine pixel sampling of 144 pixels/arcsec or 0.007 arcsec/pixel (this oversampling of the images was imposed for the dark-speckle experiment). The detector is a cooled CP20 photon-counting camera (Abe et al. 1998) allowing single photon detection with a very low dark count ($< 5\ 10^{-3}$ photon/pix/s). The quantum efficiency of CP20 is less than 10% at 700 nm.

Near diffraction-limited images of P Cyg ($m_v = 4.81$, S_p = B1Ia+) and 59 Cyg ($m_v = 4.74$, S_p = B1.5V) have been obtained (Fig. 1) using a broadband H_α filter ($\lambda_0 = 6563$ Å, $\Delta\lambda = 100$ Å) (Fig. 2).

2.2. Data analysis

The data consist of two sequences of 20 ms short exposures, for P Cyg, and the reference star 59 Cyg of similar magnitude and spectral type. In a preliminary step, the short exposures recorded by CP20 were cleaned for

Table 1. Turbulence characteristics derived from the wavefront sensor data of the adaptive optics system. Atmospheric parameters are given for the visible band

Star name	P Cyg	59 Cyg
Time	20:30 TU	21:23 TU
Average intensity in sub-apertures (photons)	51.567	42.830
r_0 (cm), open loop calculated with L_0	5.83	5.92
r_0 (cm), open loop calculated with L_0 and Zernike coef.	∼5.4	∼5.4
L_0 (m)	2.96	2.57
Zernike coef. (2,3), σ^2 (rad^2)	70	40
Zernike coef. (4,44), σ^2 (rad^2)	10	9

photon-centroiding electronic artifacts and then co-added to generate an equivalent long exposure of 99 s for P Cyg and 370 s for 59 Cyg. Despite the Coudé configuration of the 1.52 m telescope, rotation of the field between the two sequences was found to be negligible. We checked for non-linear effects introduced by the so-called photon-centroiding hole and camera saturation (Thiébaut 1994). It appears that the incoming flux is greatly below the saturation limit, the double-photon occurrence is absent. The total number of detected photons for the two images are very similar: 481563 for P Cyg and 416309 for 59 Cyg. A coherent peak and a broken ring, featuring a triple coma aberration, are clearly visible, but 59 Cyg's image is sharper, indicating that P Cyg's envelope is possibly resolved. This is quite visible in Fourier space, as shown in Fig. 3. The envelope of P Cyg clearly appears as the well resolved low frequency part in the visibility curve. High angular information is obtained up to about 80% of the cut-off frequency. The visibility curve is indeed clearly dominated by noise beyond that limit.

Since 59 was observed 53 minutes later than P Cyg, a variation of atmospheric conditions and/or a poor correction could be responsible for a noticeable change in the Point Spread Function (PSF) shape. From open/close loop data recorded by the wavefront sensor of BOA, we have derived seeing conditions (F.C.): intensity in sub-apertures, Fried parameter evolution, noise evolution, Zernike coefficient variance evolution, etc. Some of these relevant parameters are summarized in Table 1 for both stars. In particular, the Fried parameter (r_0) exhibits no temporal variation and remains stable around 5.4 cm between the 2 data sequences. Also, high order correction (Zernike coef. (4,44)) have similar variances in both cases, indicating similar adaptive mirror corrections for P Cyg and 59 Cyg. The largest difference appears for the tip-tilt corrections (Zernike coef. (2,3) of the Table 1). However we confirm that during the observations no saturation was detected, and we expect these modes to be correctly compensated for both stars. Furthermore, parameters such as turbulent layers altitude, mean isoplanetic angle and wind velocity indicate a very good stability of the atmospheric conditions during the two records.

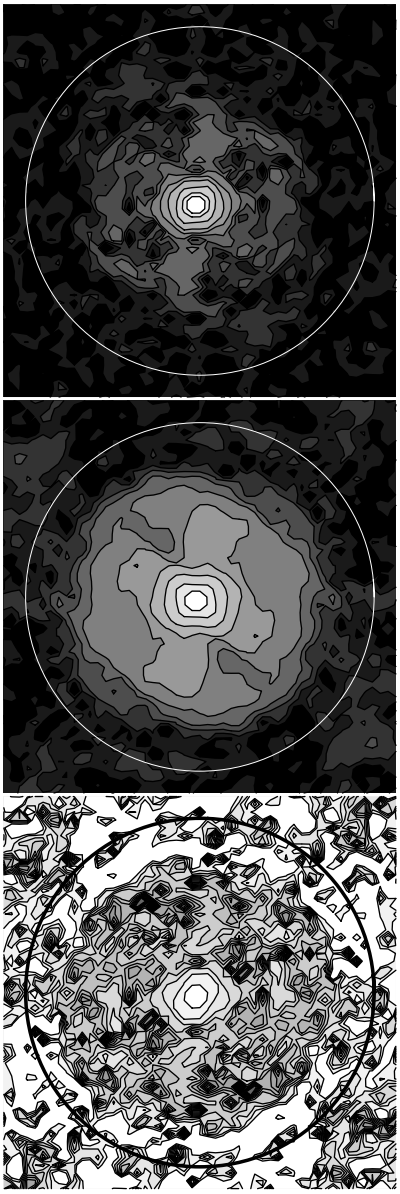

Fig. 3. Representation in contour plots of the modulus of the Fourier transform of P Cyg (top), 59 Cyg (middle) and their ratio, the visibility curve of P Cyg (bottom). The zero frequency is at the center of the images. The representations are in logarithmic scale. The circle gives the theoretical cut-off frequency of the telescope

Moreover, the photon flux stability can be checked on the short exposures statistics. For 59 Cyg, the flux is stable with a perfect Poisson variance. P Cyg's behavior is roughly the same, except for some localized empty exposures, due to electronic saturation, which have been removed.

This preliminary analysis permits us to assume that 59 Cyg can be confidently considered as P Cyg's PSF and a successful deconvolution becomes possible.

3. Image reconstruction

3.1. Deconvolution of the raw image of P Cyg

A deconvolution of the image of P Cyg using 59 Cyg as the PSF has been made using basically the iterative Richardson-Lucy algorithm (RL) (Richardson 1972; Lucy 1974) to which some improvements have been applied as we shall describe below. To improve the result, a pre-processing of the image was first performed. All images were smoothed using a moving average window of 4×4 pixels. To remove the effects of the coronagraphic mask (clearly visible in Fig. 1 at the right of P Cyg's image), only a central region of 0.9×0.9 arcsec of the smoothed images was conserved. To make the deconvolution procedure faster, the number of points of the images was further reduced by a factor of 16. The resulting images of 32×32 pixels remain correctly sampled (0.028 arcsec compared with the theoretical Shannon limit of 0.044 arcsec for the 1.52 m telescope operated at 656.3 nm).

The RL algorithm was then applied to these pre-processed images using the well-known iterative procedure:

$$x^{k+1}(r) = x^k(r) \cdot h(-r) \otimes \frac{y(r)}{h(r) \otimes x^k(r)} \qquad (1)$$

where $\otimes$ is the convolution symbol, r denotes the two-dimensional spatial position, $y(r)$ denotes the image of P Cyg, $h(r)$ the image of 59 Cyg taken as the PSF, and where $x^k(r), x^{k+1}(r)$ are the reconstructed images at the iteration k and $k+1$.

To limit the instability that appears in the solution, due to the amplification of noise, we stop the iteration number by using a comparison between the Fourier Transform of the reconstructed object at the iteration k and the Fourier transform of the image reconstructed by a Wiener filter (Lantéri et al. 1998; Lantéri et al. 1999). The main difficulty is then shifted to a correct determination of the Wiener filter. The comparison led us to choose an iteration number of 245. The result of the deconvolution is given both in grey levels and in a contour plot in Fig. 4. To make the envelope clearly visible, the contour levels are not equally spaced. The general pattern is that of a bright star, not resolved by the 152 cm telescope, surrounded by an extended envelope with bright spots.

These same results were obtained with the reconstruction RL algorithm regularized by a Tikhonov term, and in particular using the Laplacian operator (Lantéri et al. 1999). The result of this deconvolution is presented in Fig. 5 for the iteration 250 with a regularization factor equal to 0.01. Neglecting the fine structure of the envelope, a normalized circular average of the image centered on the star may be fitted by the sum of two Gaussian curves, of the form: $a\mathrm{e}^{-b|r|^2} + (1-a)\mathrm{e}^{-b'|r|^2}$ where $a \simeq 0.85$, $b \simeq 618.2$ and $b' \simeq 25.9$ if we express r in arcsec. This corresponds to an equivalent width of the envelope of about 0.4 arcsec ($\frac{2}{\sqrt{b'}}$). The radial curve is shown in a semi-logarithmic scale in Fig. 6. In this model the total integrated flux produced by the envelope ($r = (1-a)b/ab'$) was found to be about 4 times larger than the one produced by the central star. This ratio is not an absolute parameter; it depends of course on the spectral bandwidth of the experiment (Fig. 2).

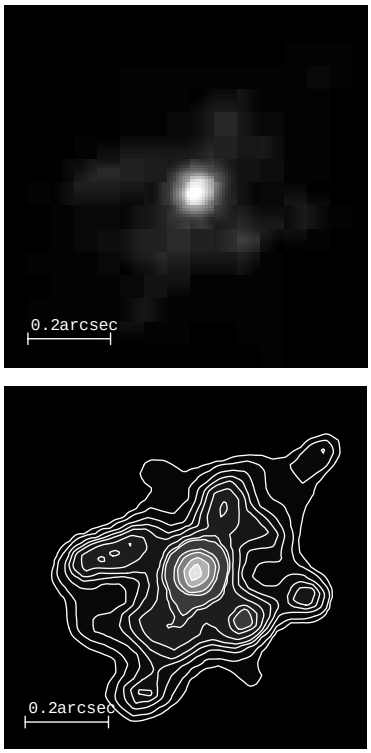

Fig. 4. Reconstructed image of P Cyg with the RL algorithm stopped at iteration 245. Top: Representation in gray levels in a linear scale. Bottom: Representation in contour plot. Contours levels are not equally spaced and correspond to: 100, 80, 60, 40, 30, 15, 12.5, 9, 6.5, 5, 3.5, 2, 1.2 percent of the image's maximum. North is at the top and East is at the right of the images. This corresponds to a rotation of 104.7° clockwise with regards to Fig. 1

We may conclude from this first analysis that the envelope of P Cyg is well resolved by the central core of the PSF of the 1.52 m telescope, corrected by the adaptive optics system. However, the envelope remains comparable in size with the residual halo of the PSF. This assumes at least that we are free of anisoplanatism problems (Fusco et al. 2000); this absence of variation allows the use of conventional deconvolution methods.

The question then may arise whether some of the fine structures we discovered in this envelope may be due to

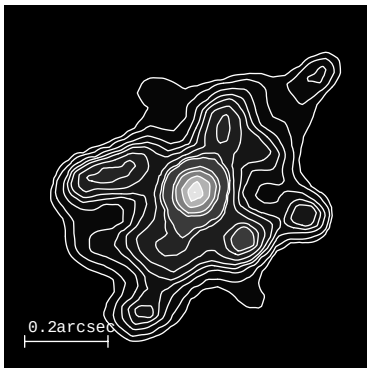

Fig. 5. Reconstructed image of P Cyg with the RL algorithm regularized by the Laplacian operator. Contours levels are not equally spaced and correspond to: 100, 80, 60, 40, 30, 15, 12.5, 9, 6.5, 5, 3.5, 2, 1.2 percent of the image's maximum. North is at the top and East is at the right of the image

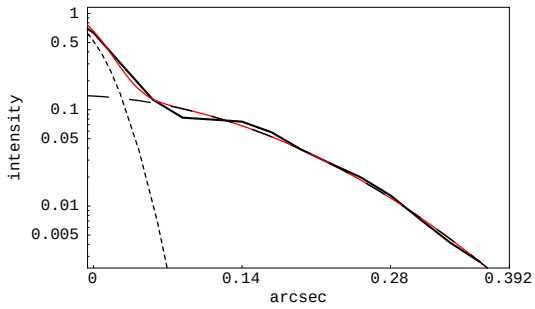

Fig. 6. Thick line: Radial profile of the object reconstructed by RL stopped at iteration 245 (image normalized to one). Dashed lines: Gaussian curves. Thin line: Sum of the two Gaussian curves. Intensity is in logarithmic scale

artifacts of the reconstruction process. A very important issue to consider, is a possible variation of the PSF during the experiment (from P Cyg to 59 Cyg), as discussed recently by Harder and Chelli (Harder & Chelli 2000). These authors show that a local non-stationary turbulence may produce strong residual aberrations (clearly visible in the first diffraction ring of their Fig. 17). At worst, we can imagine that the observed structures in our image result only from variations in the PSF, from P Cyg to 59 Cyg.

A comparison between the reconstructed image and the PSF is made in Fig. 7. To make the structures more visible, we used a representation similar to that of Harder and Chelli (Harder & Chelli 2000). The images are negatives of intensities and the representation uses threshold and saturation. Doing so, a strong (white) secondary maximum appears in the image of P Cyg, and two lower ones remain far away from the core. Moreover, Fig. 7 shows clear evidence that the central (white) surface of the reconstructed object is larger than that of the PSF (this will be interpreted in the next section as an effect of the envelope). Such a structured image can hardly result from the

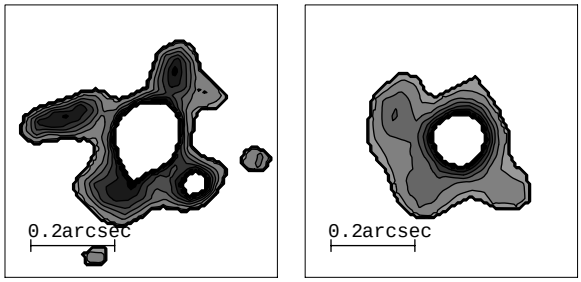

Fig. 7. Representation at the same scale of the reconstructed image of the Fig. 5 (left) and of the PSF (right) in contour plot. The white parts are due to the threshold and the saturation applied to both images: intensities lower than 6% and higher than 15% of the maximum are made white. North is at the top and East is at the right of the images

variations of the PSF. However, it is also difficult to ascertain that our reconstructed image is free of any residual error (much more data would have been necessary for this). To strengthen our confidence in the fine details of the reconstructed image of the envelope, we have implemented a series of tests and processings. They are described in Sects. 3.2 and 3.3, and in the Appendix.

3.2. Deconvolution of the envelope - independent of P Cyg

We have further processed the data assuming that P Cyg observed in H_α may be fairly represented by an unresolved star surrounded by an extended envelope. Let us write P Cyg as $e(r) + \gamma\delta(r)$, where $e(r)$ is the envelope and γ the relative intensity of the star defined by the Dirac function $\delta(r)$. The observed image is then modeled as $y(r) = e(r) \otimes h(r) + \gamma h(r)$. We have implemented a somewhat heuristic procedure that consists of subtracting $\gamma h(r)$ from $y(r)$ to obtain $e(r) \otimes h(r)$. The procedure has some similarity with the CLEAN algorithm (Högbom 1974), or the Lucy algorithm (Lucy 1994). In practice, it consists of subtracting an appropriate fraction of the image of 59 Cyg correctly shifted from P Cyg. The parameters of this subtraction are determined to leave a smooth pattern for $e(r) \otimes h(r)$, with no remaining bump or hole due to the unresolved star. We found that a fraction $\gamma = 20\%$ of the PSF ($h(r)$), shifted by ($X = -0.3$ pixels, $Y = +1.3$ pixels) was to be subtracted from P Cyg ($y(r)$). This was done using an interpolation of the images with Mathematica (Wolfram 1999). Figure 8 shows the residual blurred envelope $e(r) \otimes h(r)$ (top) and the fraction of the PSF subtracted to the image of P Cyg $\gamma h(r)$ (bottom). This procedure, performed independently of the above deconvolution and parametric estimation of the star plus envelope, led also to the same ratio 4 for the energy of the envelope relative to the central star.

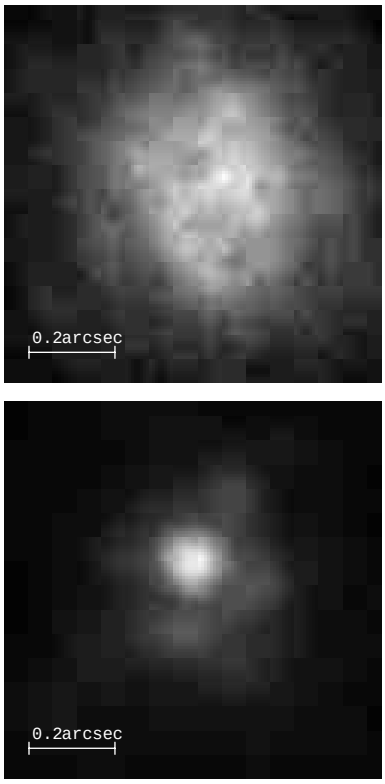

Fig. 8. Representations in grey levels of the residual blurred envelope $e(r) \otimes h(r)$ (top) and of the fraction $\gamma h(r)$ of the image of 59 Cyg subtracted from P Cyg (bottom). The sum of these two images gives back the observed image of P Cyg. The orientation is that of Fig. 1

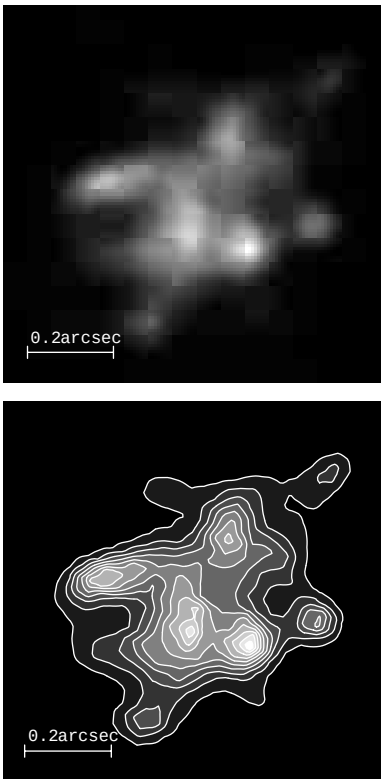

Fig. 9. Image reconstruction of the envelope of P Cyg in grey levels (top) and in contour plot (bottom). Contour levels are equally spaced. North is at the top and East is at the right of the images

We then processed the residual blurred envelope $e(r) \otimes h(r)$ using the same RL algorithm stopped at the same iteration number 245. The result is depicted both in grey levels and in a contour plot with linear contour spacing in Fig. 9. The image of the envelope is fully consistent with what was obtained in the raw deconvolution of Fig. 4. The bright spots are all found at the same position. Moreover, there is a bright spot very close to the star clearly visible in this representation in the South-West direction; it was only perceptible as a small deformation of the central star in Fig. 4.

3.3. Analysis of the quality of the deconvolution

We have implemented a few more computations to check the quality of the results we give in this paper. The whole deconvolution procedure was also performed using the Image Space Reconstruction Algorithm (ISRA) (Daube-Witherspoon et al. 1986) instead of the RL algorithm. The comparison with the image reconstructed by the Wiener filter leads us to the iteration 303. The reconstructed image is presented in Fig. 10. The two algorithms gave almost the same results, backing up the deconvolution results given in this paper.

In respect to this we may conclude that the deconvolution was carried out taking into account the problem of noise; we also made use of an a priori model, by assuming that P Cyg was the sum of an unresolved star and an envelope. An important question remains: up to what precision can we trust 59 Cyg as an accurate PSF for P Cyg? Several elements enable us to give a positive answer to that question: the seeing conditions were similar for both observations, and we found the same ratio of the flux envelope/star (about 4) before and after deconvolution. It would have been very convincing to have a series of sandwitched observations of P Cyg and a reference, eventually with different seeing conditions, and have all the results that converge towards a unique solution. In fact, we made an elementary test that consisted in dividing the long exposure of P Cyg in two sequences. The same operation was applied to 59 Cyg. We have then made a deconvolution of these four resulting images. The results are very similar to those obtained with the deconvolution presented in Fig. 4 and are not reproduced here. In an alternative we give in the appendix the results of a series of additional tests that tend to confirm 59 Cyg as a correct PSF.

Fig. 10. Reconstructed image of P Cyg with the ISRA algorithm stopped at iteration 303. Contour levels are not equally spaced and correspond to: 100, 80, 60, 40, 30, 15, 12.5, 9, 6.5, 5, 3.5, 2, 1.2 percent of the image's maximum. North is at the top and East is at the right of the image

We believe we have interpreted our current data as far as is possible. Of course, future observations, with possibly a larger telescope, will be very useful to confirm our first results and to further specify the morphology of this object.

4. Discussion

The present work follows a long series of observations to track the history of P Cyg's giant eruptions in 1600 and 1655. Following the first attempts in this direction (Feibelman 1995), it was clear that the star to its nebula brightness ratio, constitutes a challenging obstacle for the optical mapping of the nebular morphology. Indeed only few observations, with heterogeneous angular resolutions are reported in the literature. Leitherer and Zickgraf (Leitherer et al. 1987) first published the detection of P Cyg's extended nebulosity using CCD imaging. Later, Johnson et al. (Johnson et al. 1992) reported the detection of forbidden emission lines due to nitrogen enriched material at 9 arcsec. The first coronagraphic imaging of P Cyg from the ground was obtained by Barlow et al. (Barlow et al. 1994) from high resolution long-slit data. Barlow and co-workers discovered the presence of a 22 arcsec nearly circular shell which presents bright condensations of about 2 arcsec wide, mostly in the North (their plate scale is of 0.255 arcsec per pixel where a 4.3 arcsec occulting strip was used). STScl coronagraph imaging, using a 4.8 arcsec occulting disk, shows almost the same features (Nota et al. 1995). From another point of view P Cyg constitutes an ideal target for testing new and different imaging techniques. Among these there are the spectral-line image sharpening techniques SCASIS (de Vos 1994), the AMOS adaptive optics observations (Morossi et al. 1996), and occulting mask imaging (4 arcsec) with the new MOMI instrument for wide field imaging (O'Connor et al. 1998). In the latter case the authors suggest highly asymmetrical features at $3-4$ pc from the star ($7'$) probably associated with previous mass-loss events (Meaburn et al. 1999). At the same time, radio imaging now offers approximately the same panel of field and spatial resolution as optical imaging making the comparison of optical and radio maps possible. Indeed, sounding different scales in radio wavelength can easily be achieved by changing the baseline configuration of radio arrays (Skinner et al. 1998). Using this possibility, Skinner and co-workers have compared radio maps to Barlow's coronagraphic image of P Cyg (Barlow et al. 1994). These authors claim that the emissive regions in radio and visible are roughly the same, although this comparison is further complicated by the coronagraphic mask and the telescope diffraction pattern. They conclude that both radio and optical maps exhibit the same details having the same physical origin: i.e. dense clumps overtaken by the faster wind and heated by shocks.

Low and intermediate spatial resolution images suggest a global spherical expanding envelope but clumpiness is present in each case. This trend is also present at higher spatial resolution of the 250 km MERLIN centimetric network (Skinner et al. 1997) approaching the submilliarcsecond observations of the GI2T optical interferometric (Vakili et al. 1997).

In this context our present reconstructed image of P Cyg's environment in H_α presents, as expected, strongly clumped features within the 1 arcsec field of view (0.011 pc with $D = 1.8$ Kpc). More than 6 enhanced emission clumps are counted with our 0.05 arcsec spatial resolution in a nearly 0.6 arcsec region superimposed to the unresolved central star. The mean size of the clumps is roughly 0.08 arcsec which is the angular limitation of the 152 cm OHP telescope. These results agree well both in size and morphology with MERLIN observations, at nearly the same resolution. The typical diameter of emitting regions for MERLIN is 0.4 arcsec (0.13 arcsec for the core), and amazingly comparable to an optical structures (Fig. 9). In this same figure, a North-East/South-West preferential axis appears in the H_α image due to the grouping of the clumps, the distribution being otherwise rather uniform. The same orientation was also pointed out in SCASIS observations at a lower spatial resolution (de Vos 1994). Note that in our reconstructed image a bright feature is located at 80 mas South-East of the central star. We can speculate on its relation to the local strong emission discovered at 0.8 mas from the star in August 1994 by the GI2T interferometer (Vakili et al. 1997) although the E-W absolute position of the latter emission was not given by GI2T. If this scenario holds, this position, some 3.2 years later, implies a projected velocity around 110 km s^{-1}. Taking into account the radial velocity and uncertainties $208\pm$ 78 km s^{-1} obtained by Vakili et al. (Vakili et al. 1997), this projected velocity is to be expected for a clump

nearly on the line of sight ejected three years earlier with the terminal velocity, and thus, compatible with the GI2T observations. Although the possible physical relation of 1994 blob and 1997 clump remains to be robustly settled, interferometric and AO imaging repeated in the future, should enlighten such scenarios.

At present, only radio observations by Skinner et al. (Skinner et al. 1997) present confident temporal variations. In the two 6-cm MERLIN images taken in a 40 day interval, impressive changes were observed, corroborated by VLA observations. In the observed region, the wind velocity suggests a 2 year dynamical time scale, which can hardly be compared to the 6-cm flux variations. On the other hand, the recombination time scale for hydrogen atoms ($1.210^5/n_\mathrm{e}$ in years) is shorter, but not sufficient, $\sim$160 days considering a characteristic n_e of 2.8 10^5 cm^{-3} at 0.07 arcsec. This short time scale puts strong constraints on the electron density, which has to be four times larger than the surrounding envelope material. The clumpiness can explain such a time evolution if the structures are sufficiently small and dense, or if the shocks between the wind and the clumps are strong enough. The question is whether increasing resolution would reveal the same clumpiness, and if activity observed in optical and radio wavelengths is closely correlated.

Some questions arise. How can these small scale clumps be related to the 2 arcsec ones observed in the Barlow's images at 3 arcsec from the star? How can they survive over such a long distance? Do they reappear at the location we detect them?

A challenging issue is now understanding the connection between the different spatially resolved structures and their scales which needs the monitoring of the clumpiness from the star to the interstellar medium, and constrains the mass ejection dynamics. Therefore, our present observations are the first attempt to prove that an optical monitoring of the clumpiness in inner region of P Cyg's mass loss is observationally feasible. As previously pointed out (Vakili et al. 1997), the intermediate regions of P Cyg's wind, from a few stellar radii to a few parsecs can be sounded by means of AO plus coronagraphic imaging from the ground, in relation with radio observations. The dynamical time scale for optical interferometry is approximately one month, but a temporal monitoring of P Cyg by this technique requires both higher sensitivity and larger numbers of baseline orientations due to the complex structures which occur at different scales. For larger distances, the recombination time scale in the clumpy wind should produce large effects as detected in radio, and AO becomes the perfect technique to follow such activities. The brightness of P Cyg and its evolutionary time scale allow the development of a multi-site and multi-wavelength observations campaign, using AO, optical and radio interferometry to get a unified picture of P Cyg's environment physics.

Appendix A: Tests on the PSF

We have made a series of tests that tends to strengthen our confidence in the 59 Cyg's image as a correct PSF for P Cyg. These tests are negative tests in the sense that if the PSF fails to succeed one, it should be rejected as a bad PSF.

Let us assume that 59 Cyg is a good unbiased representation of the true PSF $h(r)$. Differences between the blurred reconstructed image $b(r) = h(r) \otimes x(r)$ and the observed data $y(r)$ must then be dominated by statistical noise fluctuations, with no bias term. In this relation, $x(r)$ is our best reconstructed image, as shown in Fig. 4, and $h(r)$ the PSF 59 Cyg of Fig. 1 of the body of the paper. We assume that the noise comes from a photo-detection process, and that $y(r)$ is a realization of the Poisson process of mean $b(r)$.

A.1. Test 1: Poisson-Mandel transform

The first test we have performed is a basic one, not very sensitive to the exact value of $h(r)$, but that must be verified in any case. Let us denote y and b the values taken by $y(r)$ and $b(r)$. The total probability theorem (Papoulis 1984) allows us to write the unconditional probability $P(y)$ of $y(r)$ as the sum of $P(y/b) \times P(b)$ for all b values. For the Poisson process, the conditional probability of y assuming b is $P(y/b) = \frac{b^y}{y!} \exp(-b)$ where y is an integer (the number of photons) and b a continuous value.

As a consequence, $P(y)$ is the Poisson-Mandel transform (Mandel 1959; Mehta 1970) of $P(b)$:

$$P(y) = \int_0^\infty P(b) \frac{b^y}{y!} \exp(-b) \ \mathrm{d}b. \tag{A1}$$

We have verified that our data correctly obeys relation A1. We have taken for $P(b)$ the histogram of $b(r)$, applied the above transformation and compared the result $P(y)$ with the direct histogram of the values of $y(r)$. The comparison is shown in Fig. A1. The results are consistent with the data.

A.2. Test 2: Rotations of the true PSF

The second test we have performed was to check the correctness of the small departures from circular symmetry of 59 Cyg. We use as the PSF $h_\theta(r)$ an image of 59 Cyg rotated by an angle θ. Then the deconvolution procedure is carried out as previously and leads to an image $x_\theta(r)$. The blurred image $b_\theta(r)$ is obtained as the convolution of $x_\theta(r)$ and $h_\theta(r)$, and we finally compute the Euclidean distance between $y(r)$ and $b_\theta(r)$. The results are shown in Fig. A2 in a polar plot for θ varying from 0 to 2 π. The original PSF gives the best result. If the deviation from circular symmetry was purely random, the goodness of the deconvolution would not be affected by this rotation.

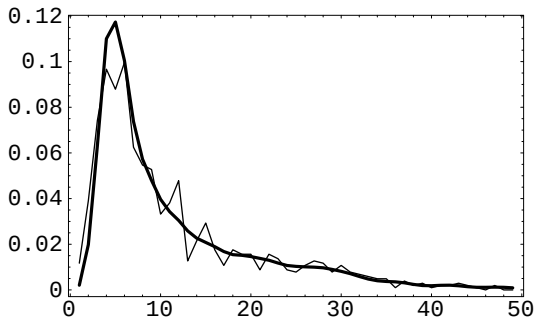

Fig. A1. Thick line: Poisson-Mandel transform $P(y)$ of $P(b)$ calculated using relation A1. Thin line: Histogram of the values of $y(r)$. A good agreement between the two curves is observed

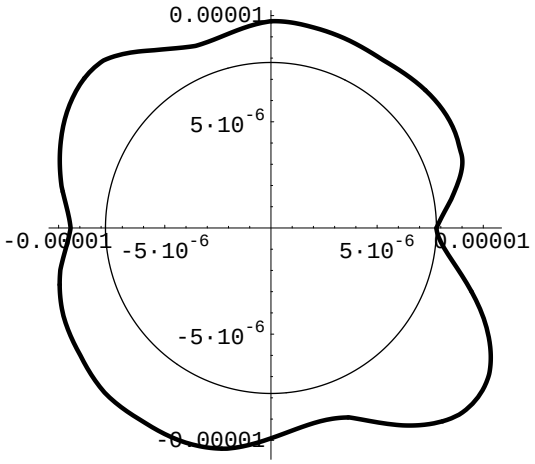

Fig. A2. Thick line: Polar plot of the Euclidean distance between $y(r)$ and $b_\theta(r)$ for θ varying between 0 and 2π. Thin line: Circle with a radius of the minimum of the Euclidean distance between $y(r)$ and $b_\theta(r)$. The minimum of the Euclidean distance is obtained for $\theta = 0$

Secondary minima of the curve appear for apparent symmetries of the PSF. Representations of the difference between $y(r)$ and $b_\theta(r)$ are shown in Fig. A3. For the sake of clarity we have represented the sign of the difference $y(r) - b_\theta(r)$. For $\theta = 0$, we get a speckle-like pattern, roughly uniform over the whole image. For other values of θ, this difference shows large patterns that indicates regions over which $b_\theta(r)$ does not correctly match $y(r)$. These trends clearly show that $h_\theta(r)$ for $\theta \neq 0$ is a biased version of $h(r)$.

As a conclusion, 59 Cyg passed the tests and could not be rejected as a bad PSF.

Acknowledgements. We wish to acknowledge A. Labeyrie for having encouraged the present work. P Cyg's observations were done using the BOA Adaptive Optics provided by ONERA to us. The manuscript benefited from discussions and critics of J.P. Véran, J. De Freitas Pacheco, G. Ricort and the GI2T team.

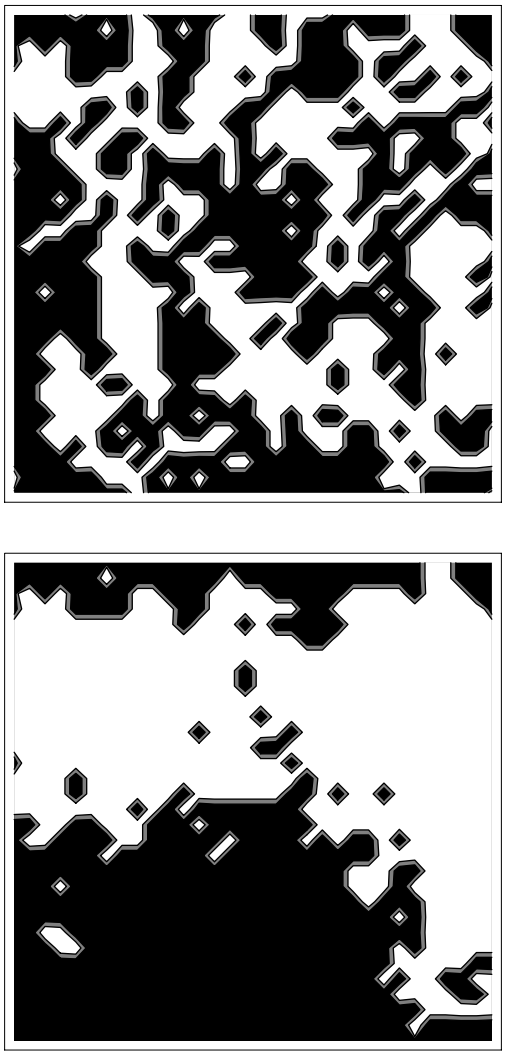

Fig. A3. Representation of the sign of the difference $y(r) - b_\theta(r)$ for no rotation of the PSF (top) and for a rotation of $\pi/2$ (bottom). This later image is not a particular case, and is characteristic of what can be obtained when the PSF is rotated

References

Abe L., Vakili F., Percheron I., Hamma S., Ragey J.P., Blazit A., 1998, in proceedings of the conference "Catching the perfect wave", Albuquerque, June 1998

Barlow M.J., Drew J.E., Meaburn J., Massey R.M., 1994, MNRAS 268, L29

Boccaletti A., Moutou C., Labeyrie A., Kohler D., Vakili F., 1998, AASS 133, 395-492

Conan J.M., Mugnier L., Fusco T., 1998, in proceedings of the Adaptive Optics and Applications, SPIE 3126

Daube-Witherspoon M.E., Muehllehner G., 1986, I.E.E.E. Trans. Med. Imaging, MI-5, 61-66

de Groot M.J.H., Lamers H.J.G.L.M., 1992, Nat 355, 422
de Vos C.M., 1993, Ph.D. Thesis, oiws.book
de Vos C.M., 1994, IAUS 158, 419
Feibelman W.A., 1995, JRASC 89, 3
Fusco T., Conan J.-M., Mugnier L.M., Michau V., Rousset G., 2000, AASS 142, 149-156
Harder S., Chelli A., 2000, AASS 142, 119-135
Högbom J.A., 1974, AASS 15, 417-426
Johnson D.R.H., Barlow M.J., Drew J.E., Brinks E., 1992, MNRAS 255, 261
Lamers H.J.G.L.M., de Groot M.J.H., Cassatella A., 1983, A&A 128, 299-310
Lamers H.J.G.L.M., Korevaar P., Cassatella A., 1985, A&A 149, 29
Lantéri H., Soummer R., Aime C., 7-11 September 1998, ESO/OSA Topical Meeting on Astronomy with Adaptative Optics, Sonthofen, Germany
Lantéri H., Roche M., Cuevas O., Aime C., 20-24 September 1999, ESO/SPIE Symposium on Remote Sensing, Florence, Italy
Lantéri H., Soummer R., Aime C., 1999, AASS 140, 235-246
Leitherer C., Zickgraf F.J., 1987, A&A 174, 103
Lucy L.B., 1974, AJ 79, 745-754
Lucy L.B., 1994, The restoration of HST images and spectra. II. Space Telescope Institute, Hanisch R.J. and White R.L. (eds.), p. 79-85
Mandel L., Proc. Phys. Soc., 74, 233
Meaburn J., López J.A., O'Connor J., 1999, ApJ 516, L29
Mehta C.L., 1970, Prog. Opt. 3, 399-428
Morossi C., Franchini M., Ragazzoni R., et al., 1996, SPIE 2828, 301
Nota A., Livio M., Clamplin M., Schulte-Ladbeck R., 1995, ApJ 448, 788
O'Connor J.A., Meaburn J., Bryce M., 1998, MNRAS 300, 411
Papoulis A., 1984, McGraw-Hill Series in Electrical Engineering, Second Edition, 30
Richardson W.H., 1972, J. Opt. Soc. Am. 62, 55-59
Skinner C.J., Exter K.M., Barlow M.J., Davis R.J., Bode M.F., 1997b, MNRAS 288, L7
Skinner C.J., Becker R.H., White R.L., Exter K.M., Barlow M.J., Davis R.J., 1998, MNRAS 296, 669
Taylor M., Nordsieck K.H., Schulte-Ladbeck R.E., Bjorkman K.S., 1991, AJ 102, 1197
Thiébaut E., 1994, A&A 284, 340-349
Turner D., Welch G., Horsford A., et al., 1999, JRASC 93, 186
Vakili F., Mourard D., Bonneau D., Morand F., Stee P., 1997, A&A 323, 183-188
Wolfram S., 1999, The Mathematica book, Fourth Edition. Cambridge University Press